Lifetime measurements in the odd-*A* nucleus ^{177}Hf

L. Knafla,[1,*] P. Alexa,[2] U. Köster,[3] G. Thiamova,[4] J.-M. Régis,[1] J. Jolie,[1] A. Blanc,[3] A. M. Bruce,[5] A. Esmaylzadeh,[1] L. M. Fraile,[6] G. de France,[7] G. Häfner,[1,8] S. Ilieva,[9] M. Jentschel,[3] V. Karayonchev,[1] W. Korten,[10] T. Kröll,[9] S. Lalkovski,[11] S. Leoni,[12] H. Mach,[13] N. Mărginean,[14] P. Mutti,[3] G. Pascovici,[14] V. Paziy,[6] Zs. Podolyák,[15] P. H. Regan,[15,16] O. J. Roberts,[5] N. Saed-Samii,[1] G. S. Simpson,[17,18] J. F. Smith,[18] T. Soldner,[3] C. Townsley,[15] C. A. Ur,[19] W. Urban,[3,20] A. Vancraeyenest,[4] and N. Warr[1]

[1]*Universität zu Köln, Institut für Kernphysik, Zülpicher Straße 77, 50937 Köln, Germany*
[2]*Department of Physics, VŠB - Technical University Ostrava, 17. listopadu 15, 70800 Ostrava, Czech Republic*
[3]*Institut Laue-Langevin, 71 avenue des Martyrs, F-38042 Grenoble, France*
[4]*Université Grenoble Alpes, CNRS, LPSC, Institut Polytechnique de Grenoble, IN2P3, F-38026 Grenoble, France*
[5]*SCEM, University of Brighton, Lewes Road, Brighton BN2 4GJ, United Kingdom*
[6]*Grupo de Fisica Nuclear and IPARCOS, Universidad Complutense de Madrid, CEI Moncloa, 28040 Madrid, Spain*
[7]*Grand Accélérateur National d'Ions Lourds, Bd Henri Becquerel, BP 55027, F-14076 Caen Cedex 05, France*
[8]*Université Paris-Saclay, CNRS/IN2P3, IJCLab, F-91405 Orsay, France*
[9]*Institute for Nuclear Physics, Technische Universität Darmstadt, Schlossgartenstr. 9, 64289 Darmstadt, Germany*
[10]*Irfu, CEA, Université Paris-Saclay, F-91191 Gif-sur-Yvette, France*
[11]*Department of Nuclear Engineering, Faculty of Physics, University of Sofia, Sofia 1164, Bulgaria*
[12]*University of Milano and INFN sez. Milano, Via celoria 16, 20133 Milano, Italy*
[13]*National Centre for Nuclear Research, ul. Hoża 69, Warsaw, Poland*
[14]*National Institute of Physics and Nuclear Engineering, Bucharest-Magurele, RO 077125, Romania*
[15]*Department of Physics, University of Surrey, Guildford GU2 7XH, United Kingdom*
[16]*National Physical Laboratory, Teddington, Middlesex TW11 0LW, United Kingdom*
[17]*Laboratoire de Physique Subatomique et de Cosmologie Grenoble, 53, rue des Martyrs, F-38026 Grenoble Cedex, France*
[18]*School of Engineering, University of the West of Scotland, Paisley PA1 2BE, United Kingdom*
[19]*Istituto Nazionale di Fisica Nucleare, Sezione di Padova, Via Marzolo 8, 35131 Padova, Italy*
[20]*Faculty of Physics, University of Warsaw, ul. Hoża 69, PL-00-681 Warsaw, Poland*

(Received 30 August 2020; accepted 21 October 2020; published 16 November 2020)

Lifetimes of low- and high-spin states in the odd-*A* nucleus ^{177}Hf were measured during the EXILL&FATIMA campaign using a spectrometer equipped with eight HPGe-Clover detectors and 16 fast-timing $LaBr_3$(Ce) detectors. For the determination of lifetimes in the pico- to nanosecond regime, the well-established generalized centroid difference method was used. Lifetimes of the $9/2^-$, $9/2^+$, $11/2^-$, $11/2^+$ states were remeasured, the lifetimes of the $13/2^-$, $17/2^-$, $13/2^+$, $15/2^+$, and $17/2^+$ states were determined for the first time and an upper limit for the $19/2^+$ state has been established. From these lifetimes absolute reduced transition probabilities were extracted and compared to particle-rotor-model calculations and quasiparticle-phonon-model calculations showing the importance of including multipole-multipole interactions in the description of odd-*A* nuclei in the rare earth region.

DOI: 10.1103/PhysRevC.102.054322

I. INTRODUCTION

The rotational structure of ^{177}Hf, arising from the decay of ^{177m}Lu, has been studied extensively in the past [1–6]. Two rotational bands with opposing parity are populated at relatively high spin and decay via a complex combination of inter- and intraband transitions [2]. This makes the nucleus ^{177}Hf a prime candidate to be investigated and probed against nuclear structure models. The general schematics of the level scheme are well described in the framework of the Nilsson model. Coupling rotational motion to single particle states gives a satisfying description of the energies of the band structure by associating the two bands with the $7/2^-[514]$ and $9/2^+[624]$ neutron orbitals, respectively [6].

The description of the intertwined electric dipole transitions between the bands is more complex. The $E1$ transitions present in ^{177}Hf are relatively strong compared to the, usually, hindered low energetic $E1$ transitions in the rare earth region [6] and cannot easily be described by the assumption of a particle coupled to rotational motion. In this model, calculated $E1$ strengths are orders of magnitude smaller than the experimental values. Calculations in the Nilsson framework were expanded to include Coriolis coupling, pairing, and

*Corresponding author: lknafla@ikp.uni-koeln.de

octupole-vibration particle coupling [4] laying the groundwork for a successful description of $E1$ transitions in odd-A rare earth nuclei. Hamamoto *et al.* [7] worked out, that even for nuclei that are stable against octupole deformation, the $E1$ strengths can only be accounted for by including a coupling to an octupole vibration [7–9]. Few lifetimes of excited states in ^{177}Hf were known and transition strengths were determined from measured intensity ratios under the assumption of constant quadrupole moment. A variety of different $B(E1)$ transition strengths are found in the literature [2–4,6,7].

With the recent advances in novel scintillator materials and improved experimental methods, direct lifetime measurements of excited states in ^{177}Hf have become accessible. In combination with an experimental setup combining the high resolution of HPGe detectors and ultrafast timing $LaBr_3$(Ce) scintillators it was made possible to disentangle the complex decay pattern and directly measure the lifetimes of higher-lying excited states in both rotational bands. Absolute reduced transition strengths directly derived from the newly measured lifetimes are compared to calculations performed in the framework of the particle-plus-rotor model (PRM) as well as compared to quasiparticle-phonon model (QPM) calculations. Comparing both calculations gives means to study the effect of the more complex Hamiltonian of the QPM approach, including multipole-multipole interaction.

II. EXPERIMENTAL DETAILS

The experiment was performed during the EXILL& FATIMA campaign, conducted at the Institut Laue-Langevin (ILL) in Grenoble, France. The EXIL&FATIMA spectrometer consisted of eight HPGe-clover detectors, mounted in a central ring around the focal position, and 16 ultrafast $LaBr_3$(Ce) (in the following denoted as $LaBr_3$) timing detectors mounted in forward and backward directions. The clover detectors were surrounded by BGO shields and were mounted at a distance of 14.5 cm around the source position, while the $LaBr_3$ detectors were mounted at 8.5 cm, as close as possible to maximize efficiency. This hybrid setup of HPGe and $LaBr_3$ detectors combines the high energy resolution of the clover detectors with the excellent time resolution of the $LaBr_3$ detectors. In this configuration a γ cascade of interest can be precisely selected by the HPGe detectors and the time difference between the populating and depopulating transition of the state of interest can be precisely measured by the $LaBr_3$ detectors. Time differences between γ rays detected in the $LaBr_3$ detectors were measured by time-to-amplitude converters (TAC). A detailed discussion of the experimental setup and the triggerless data acquisition is given in Refs. [10,11].

The lifetimes of excited states in ^{177}Hf were measured following the β decay of ^{177m}Lu. The ^{177m}Lu source consisted of 60 mg $Lu(NO_3)_3$ powder that had been activated for 1 h in a thermal neutron flux of 3.6×10^{13} cm^{-2}s^{-1} in the FRM2 reactor in Garching, Bavaria. The source was left for 4 months to let shorter-lived coproduced activities (^{176m}Lu and ^{177g}Lu) decay. During the experiment, the activity of the source was approximately 60 kBq and the measurement was conducted at focal position for 72 h. The full projections of HPGe and $LaBr_3$ threefold coincidences measured during this experiment are shown in Fig. 1 and the dominant transitions in ^{177}Hf are labeled. The level scheme of the ^{177m}Lu decay is shown in Fig. 2.

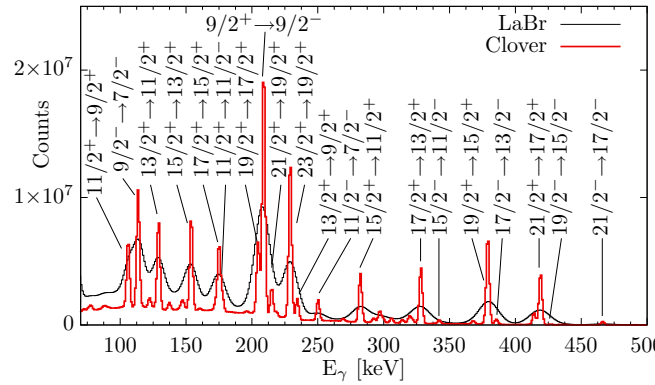

FIG. 1. Full projections of the clover (red) and $LaBr_3$ (black) threefold coincidences measured during the 72 h measurement. The clover ($LaBr_3$) spectrum is generated by using Ge-$LaBr_3$-Ge (Ge-$LaBr_3$-$LaBr_3$) events, respectively. The dominant transitions in ^{177}Hf are labeled.

III. FAST-TIMING METHOD AND DATA ANALYSIS

For the measurement of lifetimes in the sub-nanosecond regime, the well-known generalized-centroid-difference (GCD) method was used [15]. This method is based on the direct measurement of the time difference between two coincident γ rays populating and depopulating a state of interest. The feeding or decaying transition of a state of interest can either be observed by a $LaBr_3$ detector connected to the start or stop input of a TAC. If the feeding transition is detected in a start detector and the decaying transition is detected in a stop-detector, a so-called delayed time distribution is generated. If the feeding and depopulating γ rays are detected in reverse a so-called antidelayed time distribution is generated. This way, two independent time distributions are generated. Under the assumption of no background contributions, the delayed time distribution $D(t)$ is defined as the convolution of the prompt-response function (PRF) $P(t)$ of the setup and an exponential decay [16,17]:

$$D(t) = n\lambda \int_{-\infty}^{t} P(t' - t_0) e^{-\lambda(t-t')} dt' + n_r, \quad \lambda = 1/\tau, \quad (1)$$

where n is the number of counts in the time distribution, n_r are constant random counts, and τ is the mean lifetime of the excited state of interest. By definition the centroid of a time distribution $D(t)$ is shifted by the mean lifetime from the centroid t_0 of the PRF [18]. If the lifetime of the state of interest is larger than the width of the PRF a slope develops in the time spectrum that is correlated to the decay constant λ. By the GCD method the lifetime of the state of interest can be calculated from the centroid difference between the delayed and antidelayed time distribution while taking into account the combined time response of the system [15,16]

$$2\tau = \Delta C(E_{\text{feeder}}, E_{\text{decay}}) - \text{PRD}(\text{E}_{\text{feeder}}, \text{E}_{\text{decay}}). \quad (2)$$

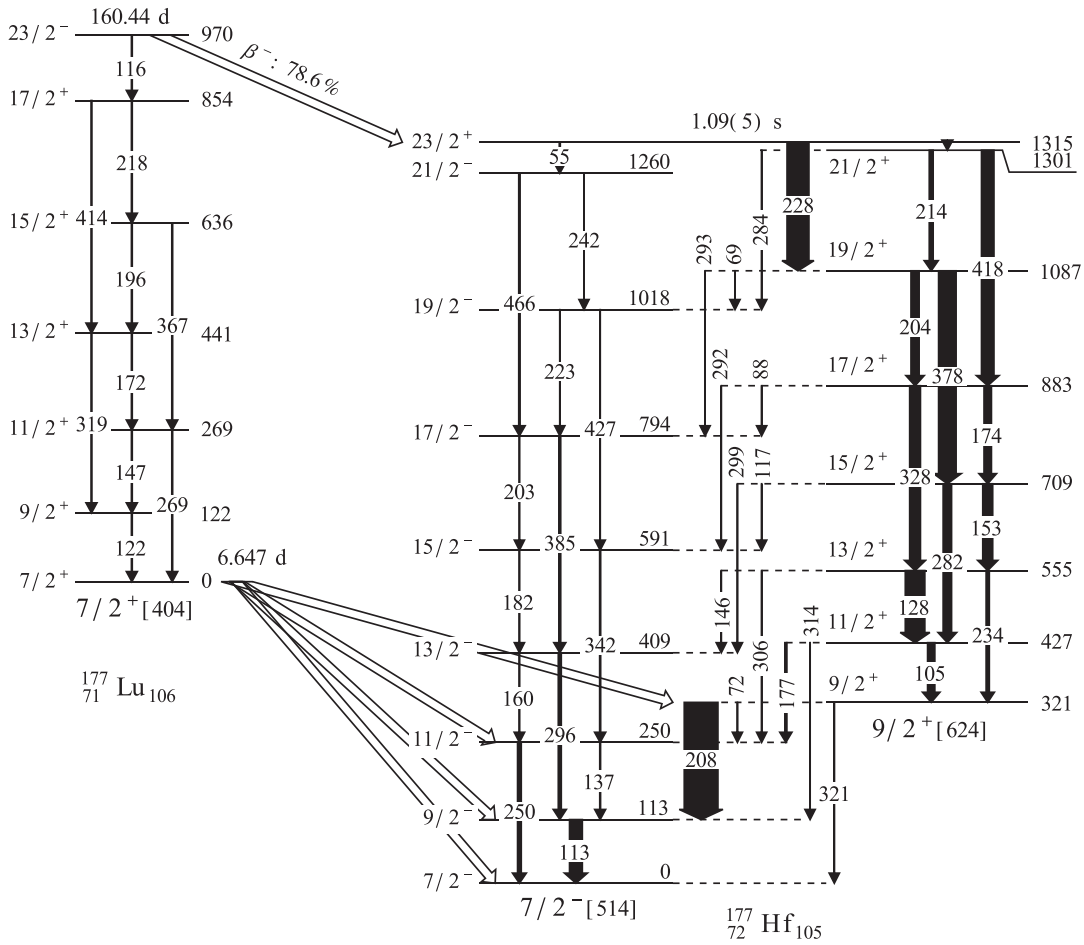

FIG. 2. Level scheme of the ^{177m}Lu decay into ^{177}Hf. Energies are given in keV and the width of the arrows corresponds to the intensity of the γ rays. Adopted from Refs. [12–14].

Two quantities have been introduced: The difference between the centroid of the delayed and antidelayed time distribution ΔC and the prompt response difference (PRD). The PRD describes the combined γ-γ time response of the system [15] and has to be calibrated to measure lifetimes. The calibration of the energy dependent PRD is performed using a standard procedure, utilizing a ^{152}Eu source and the well known lifetimes in its daughter nuclides. For a detailed description of the PRD calibration procedure see Ref. [17]. The final PRD(E_γ) curve is shown in Fig. 3 and was fitted using the function [10,17]

$$\mathrm{PRD(E_\gamma)} = \frac{\mathrm{a}}{\sqrt{\mathrm{E_\gamma + b}}} + \mathrm{cE_\gamma^2} + \mathrm{dE_\gamma} + \mathrm{e}. \tag{3}$$

The measured centroid difference is highly sensitive to the influence of Compton background from scattered coincident γ rays. These scattered γ rays have their origin in other excited states and show different, energy-dependent time responses. For the lifetime determination, the experimental centroid difference ΔC_{exp} needs to be corrected for the background time influence. In combination with the GCD method, an analytic approach to the background correction has been established to correct for the background affecting a peak of interest [16,19]:

$$\Delta C_{\mathrm{FEP}} = \Delta C_{\mathrm{exp}} + t_{\mathrm{cor}} = \Delta C_{\mathrm{exp}} + \frac{\Delta C_{\mathrm{exp}} - \Delta C_{\mathrm{bg}}}{p/b}. \tag{4}$$

The background corrected centroid difference ΔC_{FEP} is calculated from the directly measured centroid difference ΔC_{exp}, combined with a correction term t_{cor}. The background time response ΔC_{bg} is interpolated from experimental data and the peak-to-background ratio p/b is directly measured. As both peaks of interest are usually contaminated by Compton background this correction of background-related timing influence has to be applied to both the peaks correlated to the feeding and decaying transitions of interest [19]:

$$\tilde{t}_{\mathrm{cor}}(E_f, E_d) = \frac{p/b(E_d)t_{\mathrm{cor}}(E_f) + p/b(E_f)\,t_{\mathrm{cor}}(E_d)}{p/b(E_d) + p/b(E_f)}. \tag{5}$$

This represents an average of the correction terms weighted by the peak-to-background ratio and takes possibly large differences in the p/b ratio into account. The subscripts f and d denote the feeding and decaying transitions, respectively. As strong variations between peak-to-background ratios are found in the measurement presented here, a background correction according to Eq. (5) has been applied in all cases.

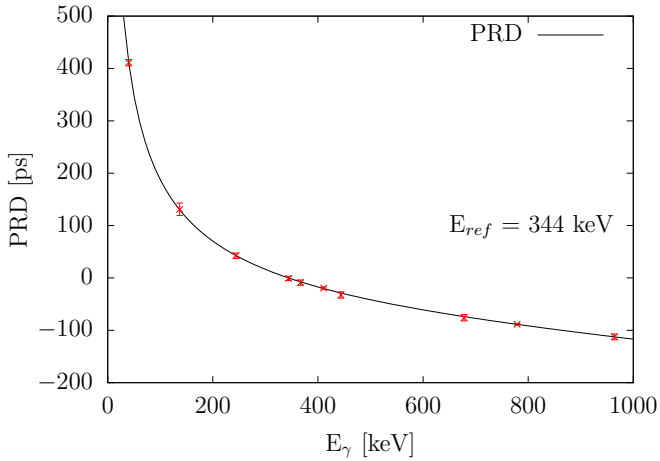

FIG. 3. Calibrated PRD curve for the EXILL&FATIMA campaign [10] derived using Eq. (3). Due to the low energy of the transitions of interest only the low energy part (below 1 MeV) of the PRD is shown. The uncertainty of the PRD is derived from a 3σ standard deviation and amounts to 5 ps.

The background corrected centroid difference is calculated by Eq. (4) with the term t_{cor} replaced by $\tilde{t}_{\mathrm{cor}}(E_f, E_d)$. The uncertainty is calculated using error propagation.

A. Lifetime measurement of the $9/2^-$ and $9/2^+$ states

The lifetimes of the $9/2^-$ and $9/2^+$ states are longer than the full width at half-maximum (FWHM) of the prompt time distribution and the convolution of the prompt time distribution with the exponential decay leads to the evolution of a slope in the time spectrum. Fitting an exponential plus a constant background to this slope directly yields the lifetime of the excited state.

Due to the entanglement of the level scheme the lifetimes of the 9/2 states are not easily accessible. The feeding $11/2^+ \rightarrow 9/2^+$ (105 keV) transition lies close to the decaying $9/2^- \rightarrow 7/2^-$ (113 keV) transition and the two peaks cannot be resolved by the scintillation detectors (see Fig. 4(a)).

By placing a clover gate to clean up the spectra it is not possible to fully remove the influence of the 105 keV and 113 keV peak from one another. Additionally, the strong $9/2^+ \rightarrow 9/2^-$ (208 keV) transition is contaminated by two different transitions. To circumvent this problem, a clover gate is placed on the $21/2^+ \rightarrow 17/2^+$ (418 keV) transition, bypassing the contaminants stemming from the $21/2^+ \rightarrow 19/2^+$ (214 keV) and $19/2^+ \rightarrow 17/2^+$ (204 keV) transitions close to the 208 keV peak. Placing the first $LaBr_3$ gate on the strong $9/2^+ \rightarrow 9/2^-$ (208 keV) transition and placing a second, broad, $LaBr_3$ gate on the peak containing both the 105 keV and 113 keV transitions, both lifetimes can be measured from the same time spectrum simultaneously (see Fig. 4(b)). The time distribution shows a slope on the left as well as on the right side. Each slope corresponds to a different energy combination with the 208 keV transition connecting the two isomers. Considering a start-stop detector combination using a stop gate set on the 208 keV transition, the combination start(105 keV)-stop(208 keV) (delayed) is responsible for the slope on the right side, while the combination stop(208 keV)-start(113 keV) is responsible for the slope on the left side of the time spectrum. Independently fitting an exponential to each side of the time distribution yields the lifetimes of the $9/2^-$ and $9/2^+$ states which amount to 776(15) ps and 1143(33) ps, respectively. The delayed time distribution shown contains around 10^5 counts and shows low background contributions emphasizing the quality of the result. To confirm the results, the lifetimes of the $9/2^-$ and $9/2^+$ states have been measured in isolation from each other. The lifetime of the $9/2^-$ state has been measured by applying a clover gate on the $21/2^- \rightarrow 17/2^-$ (466 keV) transition and using the $13/2^- \rightarrow 9/2^- \rightarrow 7/2^-$ cascade. The lifetime of the $9/2^+$ state has been measured by applying a clover gate on the $21/2^+ \rightarrow 17/2^+$ (418 keV) transition and using the $13/2^+ \rightarrow 9/2^+ \rightarrow 9/2^-$ cascade. The resulting time spectra and slope used for the determination of the lifetimes are shown in Fig. 5. In both cases, the antidelayed time spectrum has been mirrored and added to the delayed time distribution to increase statistics. The measured lifetimes for the $9/2^-$ and $9/2^+$ state amount

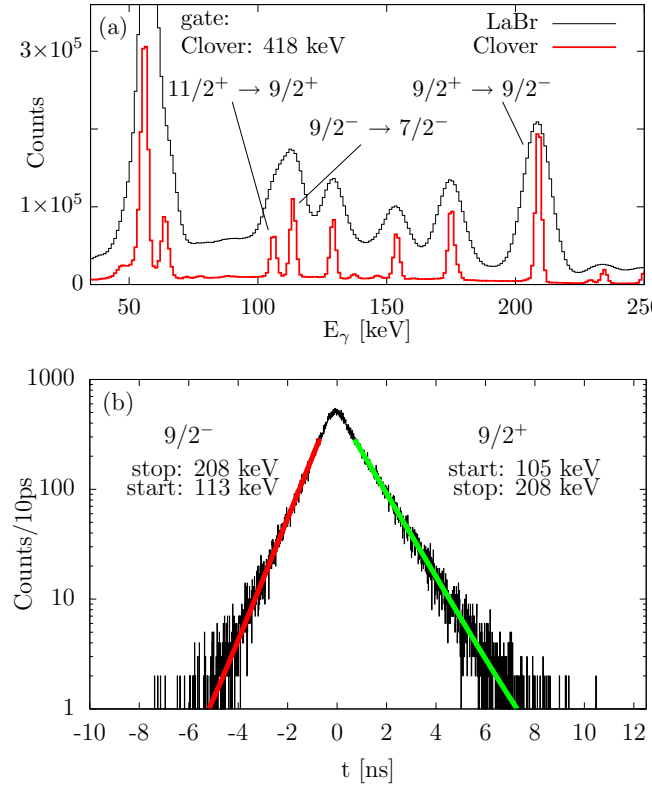

FIG. 4. (a) Gated spectra after applying a clover gate on the $21/2^+ \rightarrow 17/2^+$ (418 keV) transition. This bypasses all contaminations around the 208 keV peak of interest. (b) Time spectrum generated by applying a clover gate on the $21/2^+ \rightarrow 17/2^+$ (418 keV) transition, the first $LaBr_3$ gate on the $9/2^+ \rightarrow 9/2^-$ (208 keV) transition and a second $LaBr_3$ gate containing the $11/2^+ \rightarrow 9/2^+$ (105 keV) transitions as well as the $9/2^- \rightarrow 7/2^-$ (113 keV) transition. The lifetimes of the $9/2^+$ and $9/2^-$ states can be measured from the same time distribution.

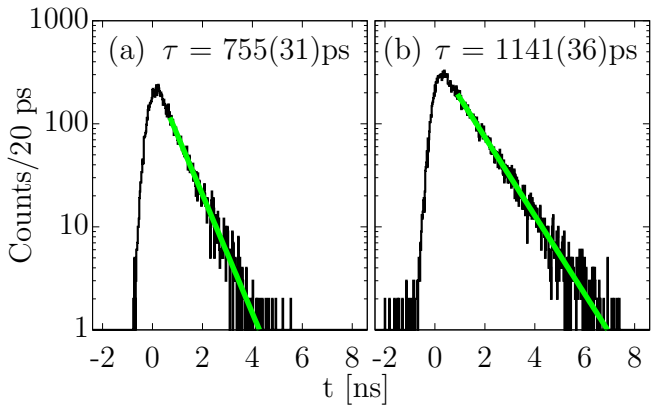

FIG. 5. Time spectrum for the lifetime measurement of the (a) $9/2^-$ and (b) $9/2^+$ states. (a) Time spectrum generated by applying a clover gate on the $21/2^- \rightarrow 17/2^-$ (466 keV) transition and placing LaBr gates on the $13/2^- \rightarrow 9/2^- \rightarrow 7/2^-$ cascade. (b) Time spectrum generated by applying a clover gate on the $21/2^+ \rightarrow 17/2^+$ (418 keV) transition and placing LaBr gates on the $13/2^+ \rightarrow 9/2^+ \rightarrow 9/2^-$ cascade.

to 755(31) ps and 1141(36) ps, respectively, in agreement with the analysis shown in Fig. 4(b).

B. Lifetime measurement of the $11/2^-$ state

Compared to the FWHM of the prompt time distribution, the lifetime of the $11/2^-$ state is short and can be directly measured using the GCD method. The lifetime analysis is performed using threefold Clover-$LaBr_3$-$LaBr_3$ coincidences. The clover gates are used to select the cascade of interest, simplifying the spectrum and significantly reducing the background. Due to the complexity of the γ-ray spectrum, gates need to be properly selected to remove disturbing peaks close to the transitions of interest. To verify that no contaminations are present in the $LaBr_3$ timing spectra, threefold Clover-$LaBr_3$-Clover coincidences are used, taking advantage of the resolution of the clover detectors to investigate the gated energy spectrum. The lifetime of the $11/2^-$ state is accessible using several different γ-γ cascades. To verify and cross-check the experimental results, all combinations of feeding and decaying transitions are analyzed, if possible. The analysis using the GCD method is exemplarily shown for the $13/2^- \rightarrow 11/2^- \rightarrow 7/2^-$ cascade. For all other cascades

TABLE I. Gates used for the analysis and the resulting lifetimes. The column labeled "HPGe gates" gives the transition on which a germanium gate was placed to clean up the spectra and in the column "$LaBr_3$ gates" the cascade of interest is shown. In cases where multiple cascades were used for the lifetime determination, the final lifetime τ_f is calculated as the weighted average with corresponding 1σ standard error.

State	HPGe gate	$LaBr_3$ gates	τ [ps]	τ_f [ps]
$9/2^-$	$21/2^+ \rightarrow 17/2^+$	$9/2^+ \rightarrow 9/2^- \rightarrow 7/2^-$	776(15)	772(14)
	$21/2^- \rightarrow 17/2^-$	$13/2^- \rightarrow 9/2^- \rightarrow 7/2^-$	755(31)	
$11/2^-$	$19/2^- \rightarrow 15/2^-$	$15/2^- \rightarrow 11/2^- \rightarrow 9/2^-$	149(13)	137(3)
	$21/2^- \rightarrow 17/2^-$	$13/2^- \rightarrow 11/2^- \rightarrow 7/2^-$	130(7)	
	$19/2^- \rightarrow 15/2^-$	$15/2^- \rightarrow 11/2^- \rightarrow 7/2^-$	136(3)	
	$17/2^- \rightarrow 13/2^-$	$13/2^- \rightarrow 11/2^- \rightarrow 9/2^-$	162(20)	
	$17/2^+ \rightarrow 13/2^+$	$13/2^+ \rightarrow 11/2^- \rightarrow 7/2^-$	141(6)	
	$19/2^- \rightarrow 15/2^-$	$11/2^+ \rightarrow 11/2^- \rightarrow 7/2^-$	137(10)	
$13/2^-$	$21/2^- \rightarrow 17/2^-$	$17/2^- \rightarrow 13/2^- \rightarrow 9/2^-$	41(3)	42(3)
	$21/2^- \rightarrow 17/2^-$	$17/2^- \rightarrow 13/2^- \rightarrow 11/2^-$	53(12)	
$17/2^-$	$13/2^- \rightarrow 9/2^-$	$21/2^- \rightarrow 17/2^- \rightarrow 13/2^-$	9(3)	9(3)
$9/2^+$	$21/2^+ \rightarrow 17/2^+$	$11/2^+ \rightarrow 9/2^+ \rightarrow 9/2^-$	1143(33)	1142(24)
	$21/2^+ \rightarrow 17/2^+$	$13/2^+ \rightarrow 9/2^+ \rightarrow 9/2^-$	1141(36)	
$11/2^+$	$19/2^+ \rightarrow 15/2^+$ $11/2^- \rightarrow 7/2^-$	$15/2^+ \rightarrow 11/2^+ \rightarrow 11/2^-$	76(10)	72(9)
	$19/2^+ \rightarrow 15/2^+$ $11/2^- \rightarrow 7/2^-$	$13/2^+ \rightarrow 11/2^+ \rightarrow 11/2^-$	62(16)	
$13/2^+$	$9/2^+ \rightarrow 9/2^-$	$17/2^+ \rightarrow 13/2^+ \rightarrow 11/2^+$	34(6)	36(3)
	$9/2^+ \rightarrow 9/2^-$	$15/2^+ \rightarrow 13/2^+ \rightarrow 11/2^+$	37(4)	
	$21/2^+ \rightarrow 17/2^+$	$17/2^+ \rightarrow 13/2^+ \rightarrow 9/2^+$	24(22)	
$15/2^+$	$9/2^+ \rightarrow 9/2^-$	$19/2^+ \rightarrow 15/2^+ \rightarrow 13/2^+$	13(6)	19(2)
	$9/2^+ \rightarrow 9/2^-$	$19/2^+ \rightarrow 15/2^+ \rightarrow 11/2^+$	19(3)	
	$9/2^+ \rightarrow 9/2^-$	$17/2^+ \rightarrow 15/2^+ \rightarrow 11/2^+$	21(4)	
$17/2^+$	$13/2^+ \rightarrow 11/2^+$	$21/2^+ \rightarrow 17/2^+ \rightarrow 13/2^+$	10(3)	10(3)
	$11/2^+ \rightarrow 11/2^-$	$21/2^+ \rightarrow 17/2^+ \rightarrow 15/2^+$	<27	
$19/2^+$	$15/2^+ \rightarrow 11/2^+$	$23/2^+ \rightarrow 19/2^+ \rightarrow 15/2^+$	<12	<12

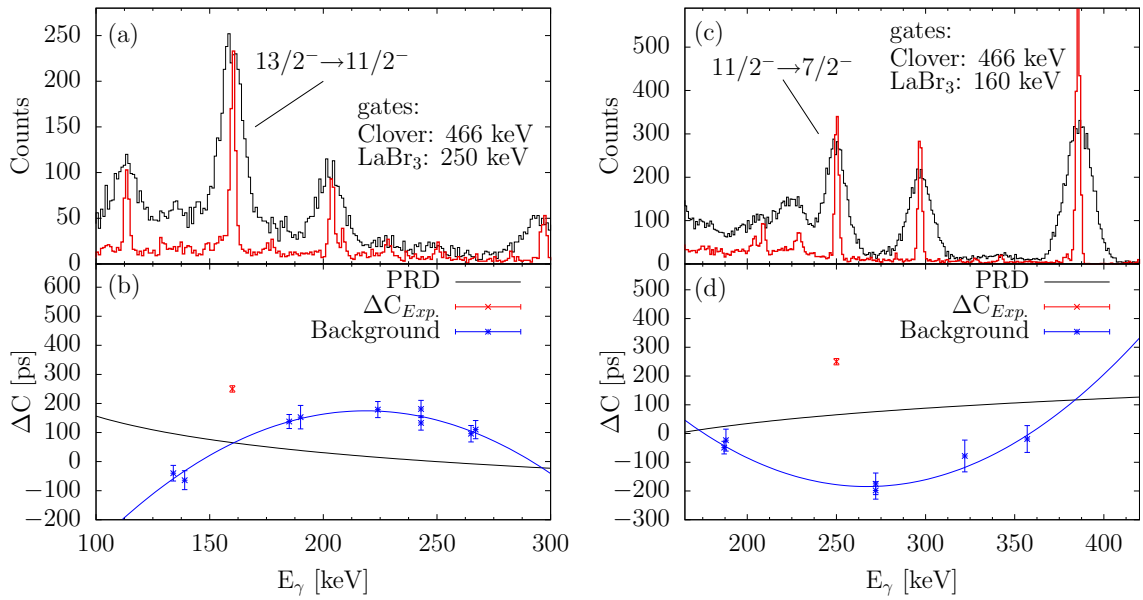

FIG. 6. Lifetime measurement of the $11/2^-$ state using the $13/2^- \rightarrow 11/2^- \rightarrow 7/2^-$ cascade. (a, c) Doubly gated clover and $LaBr_3$ spectrum with the applied gates indicated in the figures. The peaks corresponding to the feeding and decaying transition of the level of interest are free of any contaminating transition. (b, d) Measured centroid difference (red) and PRD curve (black) shifted to the energy of the applied $LaBr_3$ gate. In (blue) the measured background time response and corresponding interpolation is shown.

that were analyzed, the results of the lifetime measurement are shown with the respective cascade in Table I. To select the cascade of interest in the negative parity ground state band, a clover gate is set on the $21/2^- \rightarrow 17/2^-$ (466 keV) transition. This gate cleans up the spectra to a high degree and gives direct and isolated access to the transitions of interest. The situation after applying a $LaBr_3$ gate on the feeding (160 keV) or decaying (250 keV) transition, respectively, is shown in Fig. 6 (a,c). No contaminating peaks close to the transitions of interest can be observed. Applying the second $LaBr_3$ gate on the remaining transition of interest generates the delayed and antidelayed time distribution (shown in Fig. 7). From these time spectra the centroid difference was measured and amounts to 250(11) ps. To correct for the Compton background in Fig. 6, the background time response is interpolated for the measured energy. This is done by measuring the centroid difference in several background gates around the peak of interest. By fitting an appropriate polynomial the background time response at the full-energy peak (FEP) is determined. To successfully describe the background time response it has been shown that a second order polynomial or a function similar to Eq. (3) best describes measured data [19]. This interpolated background time response is combined with the peak-to-background ratio to correct the experimental centroid difference according to Eq. (5). In this example the lifetime of the $11/2^-$ state, after correcting for the background and taking into account the PRD, amounts to 130(7) ps.

IV. EXPERIMENTAL RESULTS

Following these procedures, the lifetimes of the $9/2^-$, $9/2^+$, $11/2^-$, $11/2^+$ states were remeasured, the lifetimes of the $13/2^-$, $17/2^-$, $13/2^+$, $15/2^+$, $17/2^+$ states were determined for the first time and an upper limit for the lifetime of the $19/2^+$ state has been established. All transitions and γ-γ cascades that were used for the analysis are listed in Table I. Due to multiple interband and intraband transitions most levels of interest can be accessed by multiple γ-γ cascades, making the analysis more complex while at the same time providing an ideal way for cross-checking the measured lifetimes. If more than one cascade was used for the lifetime determination, the final lifetime is calculated from the weighted average of all results. The final uncertainty is calculated from the 1σ standard deviation.

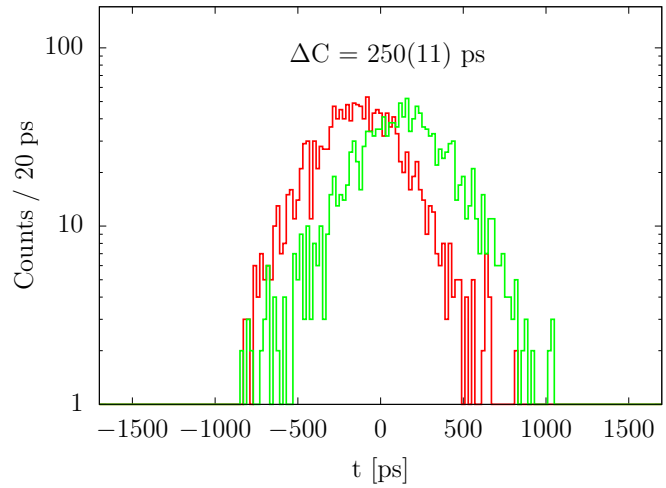

FIG. 7. Delayed and antidelayed time distribution generated from the $13/2^- \rightarrow 11/2^- \rightarrow 7/2^-$ cascade. The centroid difference amounts to 250(11) ps.

The measured lifetime of the $9/2^-$ state [$\tau = 771(13)$ ps] is in excellent agreement with the recommended value of the latest ENSDF evaluation ($\tau = 781(20)$ ps [14]) which is calculated from the results of Refs. [20–23]. The lifetime of the $9/2^+$ state measured in this work amounts to $\tau = 1142(24)$ ps. As shown in Fig. 4, the peaks of interest show a high peak-to-background ratio with no contamination from other neighboring cascades. Furthermore, the high statistics of 10^5 counts in the time distribution underline the quality of the result. Additionally, two independent cascades have been investigated to determine the lifetime. The independently measured lifetimes for the $9/2^+$ state amount to 1143(33) ps and 1141(36) ps and are in excellent agreement with each other.

Our measurement of the $9/2^+$ level lifetime differs considerably, by about 5σ, from the recommended value in the last ENSDF evaluation: 960(23) ps [14]. The latter is based on a weighted average of five mutually consistent measurements [1,24–27]. It is unusual to find such a large discrepancy from a well-established value, which renders a closer inspection of possible reasons necessary. The slope method provides a direct result and does not require PRD corrections. We also note that the $9/2^+$ level has the longest lifetime of all the levels populated in the ^{177m}Lu decay into ^{177}Hf. Thus, the accidental inclusion of other weak transitions or their Compton background into any of the gates, would lead to a reduction of the apparent lifetime, not to a prolongation.

All previous experiments were performed with fast-slow coincidence measurements, mainly using ^{177g}Lu sources. The β^- decay of ^{177g}Lu populates the $9/2^+$ level in ^{177}Hf with an endpoint energy of 175.5(8) keV and an average beta energy of 47 keV. The $M1 + E2\, 9/2^- \rightarrow 7/2^-$ transition is converted with $\alpha = 2.23$. Thus $2.23/(1 + 2.23) = 69\%$ of all 208 keV γ rays are followed by emission of a conversion electron with energies ranging from 47.6 keV to 112.9 keV. In addition 0.25% K Auger electrons with 44.8 keV and 8.5% L Auger electrons with 8.6 keV are emitted. Altogether, this spectrum of secondary atomic electrons covers a similar energy range as the primary beta spectrum and thus similar efficiencies are expected for their detection by a β detector. Also the 112.9 keV γ ray itself and the x rays emitted after the conversion electron emission will have a finite probability to trigger the β detector. Thus, for every "good" start signal from a populating β there will be 0.7 to 0.9 (depending on the exact efficiency curve of the beta detector) "false" start signals from an electron below the $9/2^-$ state. These false start signals are delayed by the lifetime of the $9/2^-$ state ($\tau = 780$ ps), i.e., they cause a left tail on the coincidence timing curve which is usually clearly separable from the right tail. Only the measurement by Vartapetyan *et al.* [28] had to consider a convolution of this effect. The other experiments had better intrinsic timing resolution which clearly separated the left and right tail.

Berlovich *et al.* [24] and Rougny *et al.* [25] used ^{177g}Lu sources and measured β-γ coincidences between a plastic scintillator detecting the beta and a NaI(Tl) scintillator detecting the depopulating 208 keV γ-ray, respectively. They found lifetimes of 995(43) ps and 938(87) ps. Hauser *et al.* [1] used the same method, but gated specifically on the high-energy part of the β spectrum to minimize the influence of conversion electrons from the (delayed) $9/2^- \rightarrow 7/2^-$ transition. They found a value of 909(72) ps.

Three more literature values are available which were not included in the evaluated ENSDF average: Vartapetyan *et al.* [28] used a triple-coincidence setup of one plastic scintillator and two NaI(Tl) detectors. The additional NaI(Tl) detector was used to impose an additional coincidence with the 113 keV γ ray at the bottom of the cascade. This effectively removes the false triggers from conversion and Auger electrons and thus the left tail. From the centroid shift with respect to the unconditioned β-γ coincidence Vartapetyan *et al.* derived a lifetime of 700(200) ps for the $9/2^+$ level, but with limited statistics.

West *et al.* [29] used EC decay of a ^{177}Ta source to populate γ-ray cascades in ^{177}Hf. The lifetime of the $9/2^+$ level was measured via a 424.7 keV–208.4 keV coincidence where both γ rays were detected by NaI(Tl) detectors. They derived a lifetime of 750(50) ps for the $9/2^+$ level.

Finally, Zhu *et al.* [30] performed an experiment combining the Gammasphere Ge detector array with additional $LaBr_3$ detectors and used a ^{177m}Lu source. Hence, the characteristics of their experiment are close to our experiment. They found a lifetime of 1050(32) ps for the $9/2^+$ level, higher than all other measurements but still 2.2 σ lower than our result.

A careful investigation of the decay schemes of ^{177g}Lu, ^{177}Ta, and ^{177m}Lu, respectively, has provided no evidence for a systematic bias towards shorter or longer lifetimes in any of the measurements. To fully understand and resolve the origin of this persisting discrepancy a new independent measurement would be required, e.g., repeating the experiments from five decades ago with a ^{177g}Lu source, but complementing the β(plastic detector)-208 keV ($LaBr_3$ detector) coincidence by an additional Ge gate on the 113 keV γ to eliminate any bias from "late" electrons stemming from the $9/2^- \rightarrow 7/2^-$ transition.

Previous measurements of the lifetime of the $11/2^-$ state were performed using Coulomb excitation [31] or utilizing the Mößbauer effect [32] and resulted in a lifetime of 154(16) ps and 153(30) ps, respectively. Both values show quite large uncertainties but are consistent with the lifetime of 137(3) ps measured in this work. This was the first direct measurement of the lifetime of the $11/2^-$ state and was determined using six independent γ-γ cascades.

In the context of a technical demonstration of the conjunction of Gammasphere with $LaBr_3$ detectors the lifetime of the excited $11/2^+$ state has been measured and amounts to 58(4) ps [30]. The lifetime measured in this work amounts to 72(9) ps. To fully isolate the relatively weak band crossing $11/2^+ \rightarrow 11/2^-$ transition, fourfold coincidences have been used. This leads to a reduction of statistics by a significant amount, which finally results in a larger uncertainty but on the other hand guarantees extremely clean spectra. Nevertheless, the lifetime determined in the Gammasphere experiment barely lies outside a 1σ uncertainty of the lifetime measured in this work. Additionally, the lifetimes of the $13/2^-$, $17/2^-$, $13/2^+$, $15/2^+$, $17/2^+$ states in ^{177}Hf have been measured for the first time and an upper limit for the lifetime of the $19/2^+$ state has been established.

V. PRM AND QPM CALCULATIONS

Calculations utilizing the particle-rotor model (PRM) have been performed to describe the basic structure of the 7/2[514] and 9/2[624] band as well as $B(E2; \Delta I = 1, 2)$ strengths. Due to the importance of the multipole-multipole interaction in the description of the electric dipole structure [7], additional QPM calculations have been performed.

The PRM is utilized as described in Ref. [33] and the calculations were performed with the computer codes GAMPN, ASYRMO, PROBAMO, and E1PROBAM that are described in detail in Ref. [34]. The Hamiltonian of the particle-plus-rotor system is a sum of the contributions of the collective rotational part, single-particle motion and pairing force:

$$H = H_{\rm sp} + H_{\rm pair} + H_{\rm core}. \tag{6}$$

The single-particle Hamiltonian $H_{\rm sp}$ describes the single-particle motion in a deformed modified harmonic oscillator (MHO) potential defined by deformation parameters ϵ_2, ϵ_4, and γ and the Nilsson parameters μ and κ. The collective rotational motion is described by the core Hamiltonian $H_{\rm core}$ that includes a Coriolis term [35]. Pairing force is treated within the standard Bardeen–Cooper–Schrieffer (BCS) approximation and is included by the $H_{\rm pair}$ term. From the Nilsson states generated for a given deformation, the strong coupling base states are calculated and all single-particle matrix elements required for the particle-rotor Hamiltonian and the calculation of transition strengths are computed [34]. For the calculations using the PRM approach only ϵ_2 is used as deformation parameter. Taking into account higher order deformation as well as γ deformation did not improve on the theoretical description and are omitted in the calculation. A first estimate for the ϵ_2 is taken from Ref. [36] and subsequently adapted to reproduce experimental transition strengths. For the separate calculations of the two rotational bands with opposing parity, 14 orbitals around the Fermi surface are selected to be included in each calculation. The pair-gap parameter $\Delta = 0.625$ MeV is calculated from the odd-even mass difference. The moment of inertia is governed by the 2_1^+ energy of the assumed even-even rotor core (^{176}Hf) and has been reduced slightly. Using this parameter, the energies of the different states are scaled down and it was modified in a way, to reproduce the level energies and band structure of interest. To reduce the effect of Coriolis coupling, the attenuation factor $\xi = 0.7$ is multiplied to all off-diagonal matrix elements [34]. The effective charge used for the calculation of reduced $E1$ strengths is calculated to be $e_{\rm eff} = -0.122e$. For the calculation of the $B(M1)$ transition strength, the collective gyromagnetic ratio g_R and effective spin g-factor $g_s^{\rm eff}/g_s$ needed to be altered. The quadrupole deformation ϵ_2, the moment of inertia and the Coriolis attenuation factor have been adjusted to reach agreement with the experimental level energies and to correctly reproduce the energy of the $9/2^+[624]$ bandhead energy. Additionally, the adjustment of the parameters aims at reproducing the experimental strength of the mixed $M1/E2; 9/2^- \rightarrow 7/2^-$ transition. The following parameters are used for the PRM calculations: $\mu = 0.4055, \kappa = 0.0636$, $\epsilon_2 = 0.235$, $\Delta = 0.625$ MeV, $E(2^+) = 0.082$ MeV, $\xi = 0.7$, $e_{\rm eff} = -0.122e$, $g_s^{\rm eff}/g_s = 0.7$, $g_R = 0.19$.

The total Hamiltonian for the QPM calculations is written as

$$H = H_{\rm intr} + H_{\rm rot}, \tag{7}$$

where $H_{\rm rot}$ is the rotational Hamiltonian. The intrinsic part $H_{\rm intr}$ of the Hamiltonian can be decomposed as [37]

$$H_{\rm intr} = H_{\rm pair} + H_{\rm sp} + H_{\rm multi}. \tag{8}$$

The $H_{\rm sp}$ part describes the deformed average mean field as in the Nilsson model. The short range monopole pairing interaction is accounted for by the pairing Hamiltonian $H_{\rm pair}$ [38]. The multipole-multipole interaction, namely the quadrupole-quadrupole ($\lambda = 2$) and octupole-octupole interaction ($\lambda = 3$) is described by

$$H_{\rm multi} = -\frac{1}{2} \sum_{\tau=p,n} \sum_{\lambda,\mu} \kappa^{\tau}_{\lambda,\mu} Q^{\tau+}_{\lambda,\mu}(\hat{r}) Q^{\tau}_{\lambda,\mu}(\hat{r}). \tag{9}$$

The deformation parameters are set to be $\epsilon_2 = 0.260$, $\epsilon_4 = -0.062$ and the neutron pairing gap $\Delta_n = 0.886$ MeV. The starting value of the deformation parameter ϵ_2 was set to be 0.250 calculated from the experimental value of $B(E2; 2_1^+ \rightarrow 0_1^+) = 183$ W.u. in ^{176}Hf [39]. The deformation parameters ϵ_2, ϵ_4 together with the neutron pairing gap Δ_n were then fitted to the energies of the seven lowest experimentally assigned band heads in ^{177}Hf [14]. The resulting values were $\epsilon_2 = 0.260$, $\epsilon_4 = -0.062$, and $\Delta_n = 0.886$ MeV. The chosen hexadecapole deformation ϵ_4 differs from that predicted by the finite range droplet model ($\epsilon_4 = 0.07$) [36] but is supported by our microscopic Skyrme + BCS calculations using the code SKYAX for the global parametrizations SV-bas and SV-min [40] that predict $\epsilon_4 = -0.04$ and by the fact that the negative ϵ_4 better fits the experimentally assigned configurations in the QPM. The oscillator-shell dependent Nilsson parameters κ and μ were taken from [41] and slightly modified for the neutron shells $N = 5$ and $N = 6$ to reproduce the experimental band head energies (for more details see Ref. [38]). The strengths of the multipole-multipole interaction were set to be $\kappa_{20} = 1.02 \times 10^{-3}$ MeV fm^{-4}, $\kappa_{22} = 1.28 \times 10^{-3}$ MeV fm^{-4}, $\kappa_{30} = 2.12 \times 10^{-3}$ MeV fm^{-6}, $\kappa_{31} = 2.15 \times 10^{-5}$ fm^{-6}, $\kappa_{32} = 2.17 \times 10^{-5}$ MeV fm^{-6}, and $\kappa_{33} = 2.40 \times 10^{-5}$ MeV fm^{-6} to fit energies of the lowest vibrational states in ^{176}Hf or taken from systematics. The inertia parameters ($A = 12.5$ keV for the $7/2^-[514]$ band and $A = 10.2$ keV for the $9/2^-[624]$ band) and the Coriolis and recoil attenuation factors, $\eta_{\rm cor} = 0.217$ and $\eta_{\rm rec} = 0.388$ were fitted to best reproduce the rotational bands in ^{177}Hf. To the improve description of high-spin states the quadratic term proportional to $[I(I+1)]^2$ was added in the rotational part of the Hamiltonian for the $7/2^-[514]$ and $9/2^-[624]$ bands. Their strengths were found to be $B = -4$ eV and $B = 2$ eV, respectively.

In the QPM framework, first the microscopic structure of the ^{176}Hf core vibrational excitations is obtained (see Table II) and electromagnetic transition amplitudes between states were calculated. From Table II one can see that the octupole phonon intrinsic state $K = 1^-$ contains about 5% of the two-quasiparticle configuration $\nu 9/2^+[624]\nu 7/2^-[514]$.

TABLE II. Microscopic structure of the lowest vibrational states in ^{176}Hf. Only components higher than 2% listed.

Vibrational state $Q_{\lambda\mu}$	2qp configuration	percentage
Q_{20}	$\nu 7/2^-[503]\nu 7/2^-[514]$	3.6%
	$\nu 11/2^+[615]\nu 11/2^+[615]$	2.2%
	$\pi 5/2^+[402]\nu 5/2^+[402]$	46%
	$\nu 1/2^+[411]\nu 1/2^+[411]$	28%
Q_{22}	$\nu 5/2^-[512]\nu 1/2^-[510]$	9.7%
	$\nu 7/2^-[514]\nu 3/2^-[512]$	5.4%
	$\pi 5/2^+[402]\pi 1/2^+[411]$	48%
	$\pi 5/2^+[402]\pi 1/2^+[400]$	6.0%
	$\pi 7/2^+[404]\pi 3/2^+[402]$	5.2%
	$\pi 3/2^+[411]\pi 1/2^+[411]$	4.8%
	$\pi 9/2^-[514]\pi 5/2^-[532]$	2.3%
Q_{30}	$\pi 7/2^-[523]\pi 7/2^+[404]$	98%
Q_{31}	$\nu 9/2^+[624]\nu 7/2^-[514]$	4.6%
	$\pi 7/2^-[523]\pi 5/2^+[402]$	84%
Q_{32}	$\nu 11/2^+[615]\nu 7/2^-[514]$	28%
	$\nu 11/2^+[615]\nu 7/2^-[503]$	8.9%
	$\nu 9/2^+[624]\nu 5/2^-[512]$	4.2%
	$\pi 9/2^-[514]\pi 5/2^+[402]$	46%
	$\pi 7/2^-[523]\pi 3/2^+[411]$	2.5%
Q_{33}	$\nu 11/2^+[615]\nu 5/2^-[512]$	31%
	$\nu 13/2^+[606]\nu 7/2^-[514]$	19%
	$\nu 13/2^+[606]\nu 7/2^-[503]$	10%
	$\nu 11/2^+[615]\nu 5/2^-[523]$	2.4%
	$\pi 11/2^-[505]\pi 5/2^+[402]$	16%
	$\pi 7/2^-[523]\pi 1/2^+[411]$	7.0%
	$\pi 9/2^-[514]\pi 3/2^+[411]$	6.5%

Subsequently, intrinsic wave functions with vibrational admixtures (see Table III) and intrinsic electromagnetic transition amplitudes are obtained. Finally, the coupling of the intrinsic and rotational degrees of freedom was taken into account. The resulting total spin-dependent wave functions are used in the calculations of the electromagnetic transitions in ^{177}Hf. The $7/2^-[514]$ band is slightly Coriolis mixed with $5/2^-[512]$ (less than 1%). The $9/2^+[624]$ band is Coriolis mixed with $11/2^+[615]$ and $13/2^+[606]$, the mixing gradually increases with increasing spin up to $19/2^+$ and reaches 30% for $11/2^+[615]$ and 15% for $13/2^+[606]$.

Fixed effective charges taking into account the center-of-mass motion were $e^{1p}_{\rm eff} = 0.593e$ and $e^{2p}_{\rm eff} = 0.991e$ for protons

TABLE III. Intrinsic structure of the two lowest band heads in ^{177}Hf calculated in the framework of QPM. Only components higher than 2% listed.

Band head	intrinsic configuration	percentage
$7/2^-[514]$	$7/2^-[514]$	73%
	$7/2^-[503]$	20%
	$13/2^+[606] \otimes Q_{33}$	3%
$9/2^+[624]$	$9/2^+[624]$	93%
	$5/2^-[512] \otimes Q_{32}$	3%

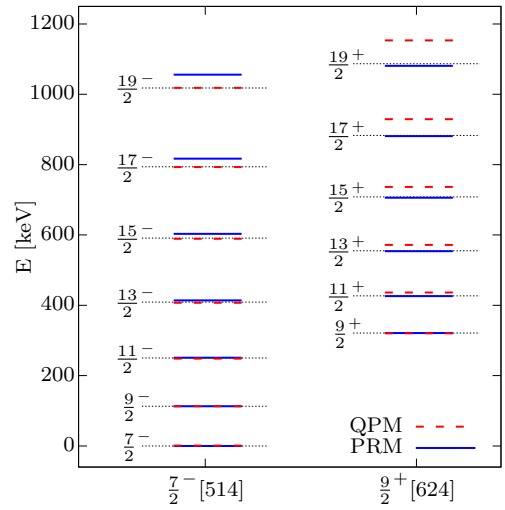

FIG. 8. Comparison of experimental and calculated level energies. The position of the experimental levels is marked as black (dotted) line and the predictions of the PRM and QPM are shown as blue (dark gray) line and red (dashed) line, respectively.

and $e^{1n}_{\rm eff} = -0.407e$ and $e^{2n}_{\rm eff} = 0.002e$ for neutrons [41]. The core intrinsic quadrupole moment $Q_0 = 734\,\mathrm{fm}^2$ and the gyromagnetic factor $g_R = 0.27$ were fixed by the experimental values for the first 2^+ state in ^{176}Hf. The remaining free parameter $g_s^{\rm eff}/g_s$ was set to 0.7.

The PRM predicts the ground state to be mostly generated by the $7/2^-[514]$ orbital with a small admixture of $5/2^-[512]$ ($\approx$6%). Further admixtures of $5/2^-[523]$ and $9/2^-[505]$ are predicted with increasing spin, but all admixtures stay below 15% up to the $19/2^-$ state. The $9/2^+$ state is predicted to be generated by the $9/2^+[624]$ orbital with some admixture of $7/2^+[633]$ ($\approx$12%). Compared to the ground state band the admixture is stronger. For increasing spin the PRM predicts an additional small admixture of $5/2^+[642]$ and a stronger admixture of $11/2^+[615]$ (25% admixture for the $19/2^+$ state).

Both the negative $7/2^-$ and positive $9/2^+$ rotational bands are well described by the PRM calculations with the $9/2^+$ band head placed at the correct energy (see Fig. 8). A Coriolis attenuation factor was required to reproduce the structure of the positive parity band. The $9/2^+[624]$ orbital origins from the $i_{13/2}$ intruder and is therefore strongly affected by Coriolis coupling compared to the $\nu 7/2^-[514]$ orbital originating from $f_{7/2}$ [6]. As the two bands are differently affected by Coriolis coupling, the attenuation is too strong for the high spin negative parity band members. Nevertheless, the theoretical PRM description of the $7/2^-[514]$ band remains in good agreement with the experimental energies. The directly measured lifetimes presented in this work were used to calculate absolute reduced transition strengths. All branching and mixing ratios were taken from Ref. [14] and conversion coefficients were calculated by BrIcc [42]. In Fig. 9 the comparison of experimental $B(M1/E2)$ to the theoretical values from the PRM and QPM calculations are shown. The experimental $B(M1)$ and $B(E2)$ transition strengths in the negative parity band are well described by the PRM calculations. For both

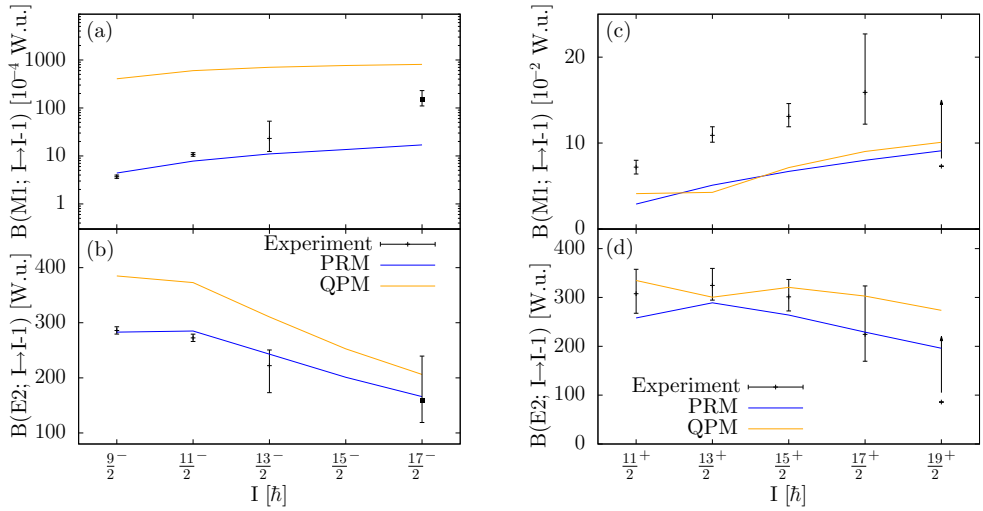

FIG. 9. Comparison of experimental and calculated $B(M1)$ and $B(E2)$ transition strength for the mixed $M1/E2 I \rightarrow I-1$ transitions in the (a,b) $7/2^-[514]$ negative parity band and (c,d) $9/2^+[614]$ positive parity band. (a,b) No mixing ratio for the $B(M1/E2; 17/2^- \rightarrow 15/2^-)$ transition is given in the literature. The filled squares give the transition strengths in the limit of pure $M1$ or $E2$ transition, respectively.

the $B(M1)$ and $B(E2)$ strengths, the experimental values are reproduced and the theoretical values follow the trend of the experimental data. The QPM calculation for the negative parity band slightly overestimates the $B(E2)$ strengths and is orders of magnitude too large for the description of the $B(M1)$ strengths. By artificially lowering the g_s and g_R factors, the theoretical $B(M1)$ values could be reduced by a factor of 5. An about 50 times lower strength is obtained by removing the admixture of the $7/2^-[503]$ orbital in $7/2^-[514]$ that is predicted by the QPM.

No mixing ratio for the $17/2^- \rightarrow 15/2^-$ transition is known in the literature. To put the measured lifetime in the context of the calculations, the transition strengths in the pure $M1$ and pure $E2$ limits have been calculated and are shown in Fig. 9 as black squares. A mixing ratio of $|\delta| \approx 3$ would be required to reproduce the $B(M1; 17/2^- \rightarrow 15/2^-)$ strength in the PRM framework. Such a mixing ratio is consistent with the known mixing ratios of the $11/2^- \rightarrow 9/2^-$ and $13/2^- \rightarrow 11/2^-$ transitions [14]. We verified moreover that a consistent application of $\delta = 3(1)$ for the $15/2^- \rightarrow 13/2^-$, $17/2^- \rightarrow 15/2^-$, and $19/2^- \rightarrow 17/2^-$ transitions provides, within experimental uncertainties, matching γ intensity balances for all levels of the negative parity band (all other involved $E1$ and $E2$ transitions with unknown mixing ratio were assumed as pure).

The theoretical calculations are able to describe the experimental $B(M1/E2; I \rightarrow I-1)$ strengths in the positive parity band. Both the PRM and QPM calculations underestimate the $B(M1)$ strengths slightly, but the theoretical values are the same order of magnitude. The strength of the $B(M1/E2; 19/2^+ \rightarrow 17/2^+)$ is given as a lower limit, calculated from the upper limit of the lifetime of the $19/2^+$ state. This makes it difficult to identify the trend of the $B(M1)$ strengths for high spins. The $B(E2; I \rightarrow I-1)$ strengths can be interpreted as decreasing with increasing spin while the assumption of increasing magnetic contribution to the transition is not supported by the data. The structure of the $E2; I \rightarrow I-2$ transitions is well described by both calculations (see Fig. 10). As no lifetime measurements for the $15/2^-$ state are feasible the corresponding data point is, un-

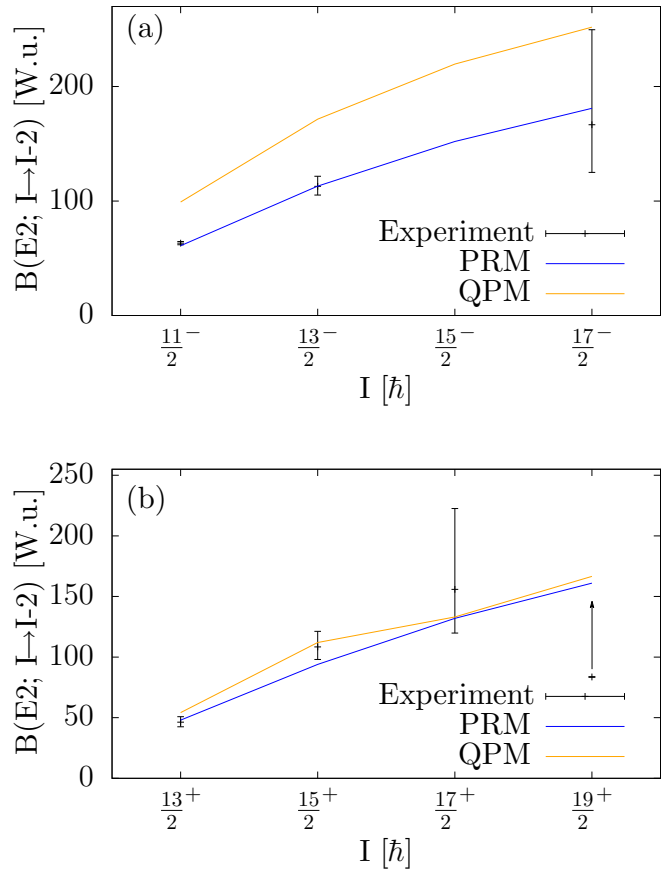

FIG. 10. Comparison of experimental and calculated $B(E2; I \rightarrow I-2)$ transition strengths in the (a) $7/2^-[514]$ negative parity band and (b) $9/2^+[614]$ positive parity band. Only a lower limit is given for the $B(E2; 19^+ \rightarrow 17/2^+)$ value.

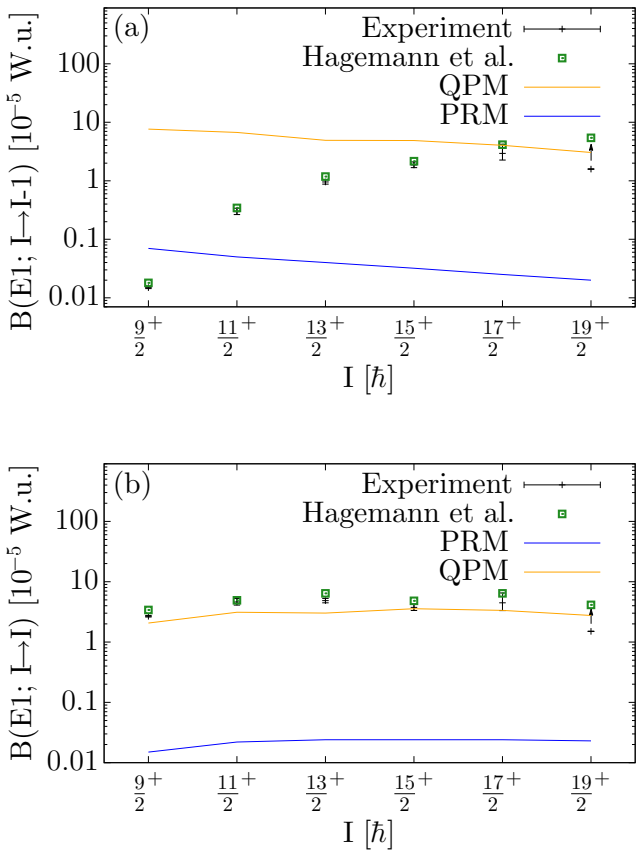

FIG. 11. Comparison of experimental and theoretical (a) $B(E1; I \to I-1)$ and (b) $B(E1; I \to I)$ values. Note the logarithmic scale of the y axis. The experimental strengths deduced in this work are compared to values gathered by Hagemann *et al.* [8].

fortunately, missing. The $B(E2; I \to I-2)$ transitions of the negative parity band are well reproduced by the PRM calculation while the QPM calculation slightly overestimates the strengths. For the positive parity band, the QPM calculations describe the experimental data in a similar way to the PRM calculations. Still, only a lower limit for the strengths of the $B(E2; 19/2^+ \to 15/2^+)$ transition can be determined. Comparison between the $B(E2; I \to I-2)$ and $B(E2; I \to I-1)$ strengths appears to show an inversely proportional relationship. With increasing spin the $B(E2; I \to I-2)$ strengths clearly increase while the $B(E2; I \to I-1)$ strengths can be interpreted as showing a decreasing trend. Assuming the $B(E2; I \to I-1)$ strengths are decreasing for increasing spin, the $B(E2; I \to I-2)/B(E2; I \to I-1)$ ratio is similar to the ratio of squared Clebsch-Gordan coefficients, closely following the behavior indicated by the Alaga rules. The $B(E1)$ strengths discussed in this work are calculated from directly measured lifetimes. Previous discussions of the $E1$ strengths in ^{177}Hf were based on $B(E1)$ values estimated on the assumption of constant quadrupole moments and measured $B(E1)/B(E2)$ branching ratios and a broad range of different $B(E1)$ values are found in the literature [2–4,6,7]. In Fig. 11 the transition strengths directly deduced from measured lifetimes are compared to the theoretical predictions of the PRM and QPM as well as to $B(E1)$ values compiled by Hagemann *et al.* [8] which are based on the values from Ref. [6]. Transition strengths calculated under the assumption of ^{177}Hf being a good rotor with constant quadrupole moment systematically underestimate the experimental strength of the $B(E1; I \to I-1)$ and $B(E1; I \to I)$ transitions. As discussed by Hamamoto *et al.* [7] the calculations using a model with a quasiparticle coupled to a rotor cannot account for the $B(E1)$ strength in ^{177}Hf. $E1$ transition strengths from the PRM calculations are orders of magnitude smaller than experimental values. In contrast, the QPM calculation, invoking vibrational excitation, is able to reproduce the magnitude of the $B(E1)$ strengths to a high degree. The strengths of the $E1; I \to I$ transitions are excellently reproduced by the QPM calculations and follow the trend of the experimental strengths. In the case of the $E1; I \to I-1$ transitions, the QPM calculation does not reproduce the observed increase in transition strengths for increasing spin. As discussed in Refs. [6,7,43], this $I_i(I_i+1) - I_f(I_f+1)$ dependency is understood in terms of Coriolis mixing. For higher I_i the effect of this dependency is reduced and the magnitude of $B(E1; I \to I-1)$ strengths is again well reproduced by the QPM calculations.

The successful description of the electric dipole transitions by the QPM calculations underlines the importance of including octupole-vibrational admixtures.

VI. CONCLUSIONS

Several lifetimes of excited states in the $7/2^-[514]$ and $9/2^+[624]$ bands of ^{177}Hf were measured following the β decay of ^{177m}Lu, using the GCD fast-timing method with the EXILL&FATIMA spectrometer. The lifetimes of the $9/2^-$ and $11/2^-$ states are in agreement with previous known measurements. The measured lifetime of the $9/2^+$ state is significantly larger than previously measured but high statistics and clean spectra emphasize the result of this work. Additionally, lifetimes of the $13/2^-$ and $17/2^-$ states in the $7/2^-[514]$ negative parity band have been measured for the first time. Concerning the $9/2^+[624]$ positive parity band, lifetimes of the $13/2^+$, $15/2^+$, and $17/2^+$ states were measured for the first time and an upper limit for the lifetime of the $19/2^+$ state has been established. These directly measured lifetimes were used to calculate transition strengths to probe against PRM and QPM calculations. The simple PRM approach gives satisfying description of the general structure concerning pure $E2; I \to I-2$ and mixed $M1/E2; I \to I-1$ transitions, but breaks down in the description of the strengths of $E1$ transitions. The successful description of the experimental $E1$ strengths by the QPM calculations again underlines the importance of considering the effect of multipole-multipole interaction, namely octupole-octupole interaction, in the description of electric monopole strengths in the rare earth region.

ACKNOWLEDGMENTS

The EXILL&FATIMA campaign would not have been possible without the support of several services at the ILL and the LPSC of Grenoble. We are grateful to the EXOGAM

collaboration for the loan of the detectors and to GANIL for assistance during installation and dismantling of the array. We are also grateful for the provision of high-quality fast-timing equipment by the FATIMA collaboration. We thank the team of the FRM2 reactor (Garching, Bavaria) for the irradiation producing the ^{177m}Lu source and Mark Harfensteller and Richard Henkelmann (ITG Garching) for the organization of the irradiation and shipment. This work was supported by the German BMBF under Grant No. 05P19PKFNA; the Spanish government through Grant No. RTI2018-098868-B-I00 and the STFC(UK). P.A. acknowledges the financial support by Project No. SP2020/45.

[1] U. Hauser, K. Runge, and G. Knissel, Nucl. Phys. **27**, 632 (1961).
[2] P. Alexander, F. Boehm, and E. Kankeleit, Phys. Rev. **133**, B284 (1964).
[3] A. Haverfield, F. Bernthal, and J. Hollander, Nucl. Phys. A **94**, 337 (1967).
[4] F. Bernthal and J. Rasmussen, Nucl. Phys. A **101**, 513 (1967).
[5] H. Hübel, C. Günther, K. Krien, H. Toschinski, K.-H. Speidel, B. Klemme, G. Kumbartzki, L. Gidefeldt, and E. Bodenstedt, Nucl. Phys. A **127**, 609 (1969).
[6] A. Bohr and B. R. Mottelson, *Nuclear Structure Volume II: Nuclear Deformations* (W. A. Benjamin, Inc., Reading, MA, 1975).
[7] I. Hamamoto, J. Höller, and X. Zhang, Phys. Lett. B **226**, 17 (1989).
[8] G. B. Hagemann, I. Hamamoto, and W. Satuła, Phys. Rev. C **47**, 2008 (1993).
[9] I. Hamamoto, Nucl. Phys. A **557**, 515 (1993).
[10] J.-M. Régis, G. Simpson, A. Blanc, G. de France, M. Jentschel, U. Köster, P. Mutti, V. Paziy, N. Saed-Samii, T. Soldner, C. Ur, W. Urban, A. Bruce, F. Drouet, L. Fraile, S. Ilieva, J. Jolie, W. Korten, T. Kröll, S. Lalkovski, H. Mach, N. Mărginean, G. Pascovici, Z. Podolyak, P. Regan, O. Roberts, J. Smith, C. Townsley, A. Vancraeyenest, and N. Warr, Nucl. Instrum. Methods Phys. Res. A **763**, 210 (2014).
[11] M. Jentschel, A. Blanc, G. de France, U. Köster, S. Leoni, P. Mutti, G. Simpson, T. Soldner, C. Ur, W. Urban, S. Ahmed, A. Astier, L. Augey, T. Back, P. Bączyk, A. Bajoga, D. Balabanski, T. Belgya, G. Benzoni, C. Bernards, D. Biswas, G. Bocchi, S. Bottoni, R. Britton, B. Bruyneel, J. Burnett, R. Cakirli, R. Carroll, W. Catford, B. Cederwall, I. Celikovic, N. Cieplicka-Oryńczak, E. Clement, N. Cooper, F. Crespi, M. Csatlos, D. Curien, M. Czerwiński, L. Danu, A. Davies, F. Didierjean, F. Drouet, G. Duchêne, C. Ducoin, K. Eberhardt, S. Erturk, L. Fraile, A. Gottardo, L. Grente, L. Grocutt, C. Guerrero, D. Guinet, A.-L. Hartig, C. Henrich, A. Ignatov, S. Ilieva, D. Ivanova, B. John, R. John, J. Jolie, S. Kisyov, M. Krticka, T. Konstantinopoulos, A. Korgul, A. Krasznahorkay, T. Kröll, J. Kurpeta, I. Kuti, S. Lalkovski, C. Larijani, R. Leguillon, R. Lica, O. Litaize, R. Lozeva, C. Magron, C. Mancuso, E. R. Martinez, R. Massarczyk, C. Mazzocchi, B. Melon, D. Mengoni, C. Michelagnoli, B. Million, C. Mokry, S. Mukhopadhyay, K. Mulholland, A. Nannini, D. Napoli, B. Olaizola, R. Orlandi, Z. Patel, V. Paziy, C. Petrache, M. Pfeiffer, N. Pietralla, Z. Podolyak, M. Ramdhane, N. Redon, P. Regan, J. Regis, D. Regnier, O. J. Roberts, M. Rudigier, J. Runke, T. Rząca-Urban, N. Saed-Samii, M. Salsac, M. Scheck, R. Schwengner, L. Sengele, P. Singh, J. Smith, O. Stezowski, B. Szpak, T. Thomas, M. Thürauf, J. Timar, A. Tom, I. Tomandl, T. Tornyi, C. Townsley, A. Tuerler, S. Valenta, A. Vancraeyenest, V. Vandone, J. Vanhoy, V. Vedia, N. Warr, V. Werner, D. Wilmsen, E. Wilson, T. Zerrouki, and M. Zielinska, J. Instrum. **12**, P11003 (2017).
[12] K. S. Krane, C. E. Olsen, and W. A. Steyert, Phys. Rev. C **10**, 825 (1974).
[13] F. G. Kondev, S. Zhu, M. P. Carpenter, R. V. F. Janssens, I. Ahmad, C. J. Chiara, J. P. Greene, T. Lauritsen, D. Seweryniak, S. Lalkovski, and P. Chowdhury, Phys. Rev. C **85**, 027304 (2012).
[14] F. Kondev, Nucl. Data Sheets **159**, 1 (2019).
[15] J.-M. Régis, H. Mach, G. Simpson, J. Jolie, G. Pascovici, N. Saed-Samii, N. Warr, A. Bruce, J. Degenkolb, L. Fraile, C. Fransen, D. Ghita, S. Kisyov, U. Koester, A. Korgul, S. Lalkovski, N. Mărginean, P. Mutti, B. Olaizola, Z. Podolyak, P. Regan, O. Roberts, M. Rudigier, L. Stroe, W. Urban, and D. Wilmsen, Nucl. Instrum. Methods Phys. Res. A **726**, 191 (2013).
[16] J.-M. Régis, G. Pascovici, J. Jolie, and M. Rudigier, Nucl. Instrum. Methods Phys. Res. A **622**, 83 (2010).
[17] J.-M. Régis, N. Saed-Samii, M. Rudigier, S. Ansari, M. Dannhoff, A. Esmaylzadeh, C. Fransen, R.-B. Gerst, J. Jolie, V. Karayonchev, C. Müller-Gatermann, and S. Stegemann, Nucl. Instrum. Methods Phys. Res. A **823**, 72 (2016).
[18] Z. Bay, Phys. Rev. **77**, 419 (1950).
[19] J.-M. Régis, A. Esmaylzadeh, J. Jolie, V. Karayonchev, L. Knafla, U. Köster, Y. Kim, and E. Strub, Nucl. Instrum. Methods Phys. Res. A **955**, 163258 (2020).
[20] C. C. Dey, B. K. Sinha, R. Bhattacharya, and S. K. Basu, Phys. Rev. C **44**, 2213 (1991).
[21] C. C. Dey, B. K. Sinha, and R. Bhattacharya, Nuovo Cimento A **105**, 1307 (1992).
[22] I. Alfter, E. Bodenstedt, W. Knichel, J. Schüth, and R. Vianden, Z. Phys. A **355**, 363 (1996).
[23] N. D'Olympia, S. Lakshmi, P. Chowdhury, E. Jackson, J. Glodo, and K. Shah, Nucl. Instrum. Methods Phys. Res. A **728**, 31 (2013).
[24] É. E. Berlovich, Yu. K. Gusev, V. V. I'lin, and M. K. Nikitin, Zh. Eksp. Teor. Fiz. **43**, 1625 (1962) [Sov. Phys. JETP **16**, 1144 (1963)].
[25] R. Rougny, J. J. Samueli, and A. Sarazin, J. Phys. (Paris) **26**, 63 (1965).
[26] B. V. N. Rao and S. Jnanananda, Indian J. Pure Appl. Phys. **6**, 555 (1968).
[27] K. P. Gopinathan, A. P. Agnihotry, S. B. Patel, and M. S. Bidarkundi, in *Proceedings of the International Conference on Nuclear Moments and Nuclear Structure, Osaka, Japan, 1972*, edited by H. Horie and K. Sugimoto (Physical Society of Japan, Tokyo, Japan, 1973), Vol. 34(Supplement), p. 430.
[28] G. A. Vartapetyan, Zh. Eksp. Teor. Fiz. **38**, 1916 (1960).
[29] H. I. West, L. G. Mann, and R. J. Nagle, Phys. Rev. **124**, 527 (1961).

[30] S. Zhu, F. Kondev, M. Carpenter, I. Ahmad, C. Chiara, J. Greene, G. Gurdal, R. Janssens, S. Lalkovski, T. Lauritsen, and D. Seweryniak, Nucl. Instrum. Methods Phys. Res. A **652**, 231 (2011).
[31] O. Hansen, M. Olesen, O. Skilbreid, and B. Elbek, Nucl. Phys. **25**, 634 (1961).
[32] L. Dautov, Y. Lysikov, U. Makhanov, and Y. Shubnyj, Izv. Akad. Nauk SSSR, Ser. Fiz. **36**, 2544 (1972).
[33] S. Larsson, G. Leander, and I. Ragnarsson, Nucl. Phys. A **307**, 189 (1978).
[34] P. Semmes and I. Ragnarsson, The Particle + Triaxial Rotor Model: A User's Guide, presented at the Risö Hands-On Nuclear Structure Theory Workshop (1992).
[35] S. V. Nilsson and I. Ragnarsson, *Shapes and Shells in Nuclear Structure* (Cambridge University Press, Cambridge, 1995).
[36] P. Möller, A. Sierk, T. Ichikawa, and H. Sagawa, At. Data Nucl. Data Tables **109–110**, 1 (2016).
[37] J. Kvasil, R. K. Sheline, V. O. Nesterenko, I. Hřivnáčová, and D. Nosek, Z. Phys. A **343**, 145 (1992).
[38] P. Alexa, Z. Hons, and J. Kvasil, J. Phys. G **36**, 045103 (2009).
[39] M. Basunia, Nucl. Data Sheets **107**, 791 (2006).
[40] P. Klüpfel, P.-G. Reinhard, T. J. Bürvenich, and J. A. Maruhn, Phys. Rev. C **79**, 034310 (2009).
[41] V. G. Soloviev, *Theory of Complex Nuclei* (Pergamon Press, Oxford, 1976).
[42] T. Kibédi, T. Burrows, M. Trzhaskovskaya, P. Davidson, and C. Nestor, Nucl. Instrum. Methods Phys. Res. A **589**, 202 (2008).
[43] T. Hayakawa, Y. Toh, M. Oshima, M. Matsuda, Y. Hatsukawa, N. Shinohara, H. Iimura, T. Shizuma, Y. Zhang, M. Sugawara, and H. Kusakari, Phys. Lett. B **551**, 79 (2003).